Chin. Phys. Lett. **39**, 056102 (2022) **Express Letter**

Pressure-Driven Ne-Bearing Polynitrides with Ultrahigh Energy Density

Lulu Liu(刘璐璐)[1,2], Shoutao Zhang(张守涛)[3*], and Haijun Zhang(张海军)[1,2*]

[1]*National Laboratory of Solid State Microstructures, School of Physics, Nanjing University, Nanjing 210093, China*
[2]*Collaborative Innovation Center of Advanced Microstructures, Nanjing University, Nanjing 210093, China*
[3]*Centre for Advanced Optoelectronic Functional Materials Research and Key Laboratory for UV Light-Emitting Materials and Technology of Ministry of Education, Northeast Normal University, Changchun 130024, China*

(Received 23 March 2022; accepted 15 April 2022; published online 23 April 2022)

Neon (Ne) can reveal the evolution of planets, and nitrogen (N) is the most abundant element in the Earth's atmosphere. Considering the inertness of neon, whether nitrogen and neon can react has aroused great interest in condensed matter physics and space science. Here, we identify three new Ne–N compounds (i.e., NeN_6, NeN_{10}, and NeN_{22}) under pressure by first-principles calculations. We find that inserting Ne into N_2 substantially decreases the polymeric pressure of the nitrogen and promotes the formation of abundant polynitrogen structures. Especially, NeN_{22} acquires a duplex host-guest structure, in which guest atoms (Ne and N_2 dimers) are trapped inside the crystalline host N_{20} cages. Importantly, both NeN_{10} and NeN_{22} not only are dynamically and mechanically stable but also have a high thermal stability up to 500 K under ambient pressure. Moreover, ultra-high energy densities are obtained in NeN_{10} (11.1 kJ/g), NeN_{22} (11.5 kJ/g), tetragonal t-N_{22} (11.6 kJ/g), and t-N_{20} (12.0 kJ/g) produced from NeN_{22}, which are more than twice the value of trinitrotoluene (TNT). Meanwhile, their explosive performance is superior to that of TNT. Therefore, NeN_{10}, NeN_{22}, t-N_{22}, and t-N_{20} are promising green high-energy-density materials. This work promotes the study of neon-nitrogen compounds with superior properties and potential applications.

DOI: 10.1088/0256-307X/39/5/056102

Exploring the behavior of inert elements including He, Ne, Ar, Kr, and Xe is the key to understanding the formation and evolution of planets.[1,2] These inert elements generally exist in gaseous form since they have typical closed-shell structures and can hardly react with other elements or compounds under ambient conditions. However, Dong *et al.* have successfully synthesized a stable Na_2He compound under high pressure.[3] Recently, many theoretical works reported that the inert gas may react with other elements or compounds under high-pressure conditions (such as iron,[4] iron peroxide,[5] alkali metal oxide, sulfide compound,[6] alkaline earth metal fluoride,[7] or H_2O[8–11]), which indicate that inert-element-stored compounds may exist in the planet's interior. Moreover, these compounds exhibit interesting properties, such as plastic and superionic states, which lead to potential applications in materials science.[8–11] Thus, an increasing number of theoretical and experimental studies have been committed to investigating the compounds with inert elements.[12–15]

Nitrogen is the most abundant element in the Earth's atmosphere and exists as the stable gaseous form of N_2 molecules with the strong triple N bond (N≡N) under ambient conditions. Because of the energy difference between a single bond (∼160 kJ/mol) and a triple bond (∼1 MJ/mol),[16] it is difficult to convert N_2 molecules into polymeric nitrogen. On the other hand, polynitrogens with N–N single bonds can produce a large amount of energy and N_2 when they are thermally decomposed. Meanwhile, the rapid release of N_2 causes high pressure. Therefore, polynitrogens with N–N single bonds as high-energy-density materials may have important potential applications for military, industry, and engineering,[17,18] and have become a hot spot in the field of new green energy sources.

Numerous efforts have been made to obtain polymeric nitrogen. The single-bonded cubic gauche phase (cg-N) of nitrogen was first predicted,[19] and then was confirmed by experiments using laser-heated diamond anvil cells at a temperature above 2000 K and under the pressure above 110 GPa.[20] Subsequent works also reported various polynitrogens under high-pressure conditions, such as layered $Pba2$,[21] cage-like diamond N_{10},[22] metallic $P4/nbm$ nitrogen,[23] single-bonded nitrogen,[24] and black-phosphorus-structure polynitrogen.[25,26] However, synthesizing these polynitrogens require extremely high pressure and some are thermally metastable under ambient conditions. So far, much attention has been focused on the lower-pressure limits of thermodynamic sta-

*Corresponding authors. Email: zhanghj@nju.edu.cn; zhangst966@nenu.edu.cn
© 2022 Chinese Physical Society and IOP Publishing Ltd

bility of metal nitrides.[27–32] Unfortunately, these metal nitrides do not contain pure nitrogen covalent bonds, but a mixture of ionic bonds and nitrogen covalent bonds. The result is that the energy density is not enough high for industrial applications. A remarkable observation is that inserting noble elements into the nitrogen system can significantly change the long-range Coulomb interactions and reduce the synthesis pressure of polynitrogen compounds.[7] For instance, solid van der Waals (vdW) compound $He(N_2)_{11}$ was synthesized under a low pressure (9 GPa) at room temperature.[33] Thereafter, many inert elements-nitrogen compounds with high-energy densities have been predicted, including HeN_4,[34] HeN_{10},[35] and XeN_6.[15] As an important member of inert elements, Ne atoms not only can trace the internal evolution of stars and the formation of solar nebulae,[2] but also have an electronic structure similar to nitrogen, which allows Ne atoms to possibly occupy vacancies in the nitrogen polymer network. The solid vdW compound $(N_2)_6Ne_7$ with guest-host structure was successfully synthesized at the room temperature and at pressure of 8 GPa,[36] but not found to contain polymeric nitrogen. It is still uncertain whether Ne and N can form new compounds with polymeric nitrogen under pressure.

In this work, to search for Ne-containing polynitrides, we systematically explored the Ne–N system under pressure via swarm-intelligence structure search. Three new Ne–N compounds with polymeric nitrogen are found: $R\bar{3}m$ NeN_6, $P6_3/m$ NeN_{10}, and $I4/m$ NeN_{22}. The *ab initio* molecular dynamics (AIMD) simulations and phonon spectra indicate that $P6_3/m$ NeN_{10} and $I4/m$ NeN_{22} are mechanically and dynamically stable above 500 K under the ambient pressure. In particular, after removal of Ne or Ne and N_2 dimers from NeN_{22}, the unique pure tetragonal polymeric nitrogen structures, t-N_{22} and t-N_{20} are obtained, and they are dynamically and thermally stable upon decompression to the ambient pressure. Remarkably, the energy densities of $P6_3/m$ NeN_{10}, $I4/m$ NeN_{22}, t-N_{22}, and t-N_{20} are found to be 11.1, 11.5, 11.6, and 12.0 kJ/g, respectively, indicating that they are promising high-energy-density materials.

Calculation Details. For the crystal structure search, we employed the unbiased swarm intelligence structure prediction method as implemented in the CALYPSO code.[37,38] Its validity has been widely confirmed by a variety of systems, from element solids to binary and ternary compounds.[39–42] Structural optimizations and electronic property calculations were performed in the framework of the density functional theory within the Perdew–Burke–Ernzerhof (PBE)[43] of generalized gradient approximation[43] as implemented in the VASP package.[44] The PBE functional was applied to all the calculations, and we have optimized the NeN_{22} at 1 atm with the local-density-approximation functional. The resulting lattice parameters of NeN_{22} are $a = b = c = 6.0054$ Å, which are smaller than those ($a = b = c = 6.0869$ Å) calculated using the PBE exchange-correlation functional. The electron-ion interaction was described by means of the all-electron projector augmented wave (PAW)[45] with $2s^22p^6$ and $2s^22p^3$ valence electrons for Ne and N atoms, respectively. A kinetic-energy cutoff of 750 eV and a Monkhorst–Pack scheme[46] with a k-point grid of $2\pi \times 0.03$ Å^{-1} were adopted to ensure that total energy calculations converged to less than 1 meV per atom. To verify the dynamical stability of predicted structures, we carried out the phonon calculations via the finite displacement approach[47] as performed in the Phonopy code.[48] The vdW interactions are also taken into consideration by using DFT-D3 functional[49,50] in VASP. Using AIMD within the NPT ensemble with a Langevin thermostat.[51] The AIMD simulations were carried out within the $2\times2\times2$ (176 atoms), $2 \times 2 \times 1$ (184 atoms), $2 \times 2 \times 1$ (176 atoms), and $2\times2\times1$ (160 atoms) supercells for NeN_{10}, NeN_{22}, t-N_{22}, and t-N_{20}, respectively. AIMD simulation lasted for 7 ps with a time step of 1.0 fs, and the equilibrium structures were obtained from the last step of AIMD simulations. The electron localization function (ELF) was utilized to measure the degree of electron localization.[52] Crystal orbital Hamilton populations (COHPs)[53] as implemented in the LOBSTER program[54] was used to quantitatively characterize the chemical bonding properties. The noncovalent interactions (NCIs) in molecular structures were analyzed by the CRITIC2 code.[55,56] The steric NCIs are visualized through the Visual Molecular Dynamics software.[57]

Results and Discussion. To determine the stable Ne–N phases, we focus on nitrogen-rich NeN_x ($x = 1$–10, 22) compounds and perform structure search at 1 atm, 50 GPa, and 100 GPa. It has been shown that nitrides containing noble elements can be stabilized under high pressure mainly due to the participation of the vdW effects.[34,35] Therefore, the vdW interactions are also considered to calculate the formation enthalpies of each NeN_x structure with the lowest enthalpy at the corresponding pressure, where the formation enthalpy ΔH is defined as

$$\Delta H(NeN_x) = [H(NeN_x) - H(Ne) - xH(N)]/(1 + x). \quad (1)$$

Here, $H = U + PV$ is the enthalpy of each composition with U, P, and V being internal energy, pressure, and volume, respectively; $H(NeN_x)$ is the enthalpy per formula unit of NeN_x; $H(Ne)$ and $H(N)$ represent the enthalpy per atom of elemental Ne and N, respectively; α-nitrogen and $P4_12_12$ structures are used for pure nitrogen.[58,59] Meanwhile, $Fm\bar{3}m$ Ne as a refer-

ence phase is taken for the computation of formation enthalpy.[60] Then, the resulting ΔH of each NeN_x at selected pressure is used to build the convex hull as shown in Fig. 1(a). The thermodynamically stable compounds are located on the convex hull (solid lines), whereas compounds lying on the dotted lines are energetically unstable. According to the convex hulls shown in Fig. 1(a) and the pressure-composition phase diagram illustrated in Fig. 1(b), we found three new stable phases: $R\bar{3}m$ NeN_6, $P6_3/m$ NeN_{10}, and $I4/m$ NeN_{22}. At 1 atm, there are no compounds showing negative formation enthalpies with respect to the mixture of Ne and N_2. With an increase in pressure, NeN_6 is found to be stable at 69 GPa. As pressure further increases, NeN_{10} becomes energetically more favorable than NeN_6 or Ne and N_2 mixtures above 70 GPa, as shown in Fig. S1 in the Supporting Information. For the stoichiometry NeN_{22} with the highest N content, it becomes thermodynamic stable at a higher pressure of 76 GPa, as shown in the inset of Fig. 1(b). In addition, it should be mentioned that $(N_2)_6Ne_7$ was successfully synthesized under high pressure,[36] which offers the possibility of synthesizing our predicted Ne–N phases.

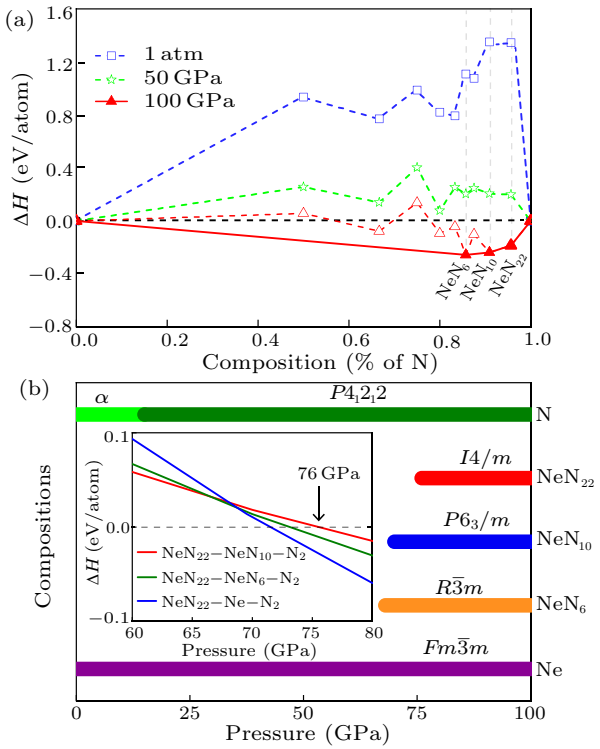

Fig. 1. (a) Convex hulls for formation enthalpies (ΔH, with respect to pure Neon and pure nitrogen) calculated by considering the DFT-D3 functional under different pressures of 1 atm, 50 GPa, and 100 GPa. (b) Pressure-composition phase diagram of the Ne–N compounds up to 100 GPa. The inset in (b) shows the enthalpy differences of $I4/m$ NeN_{22} relative to the mixtures of $R\bar{3}m$ NeN_6, $P6_3/m$ NeN_{10}, or Neon and nitrogen.

NeN_6 is predicted to stabilize into a hexagonal structure with $R\bar{3}m$ symmetry [Fig. 2(a)]. In this structure, all nitrogen atoms have the equivalent $18h$ Wyckoff position. More interestingly, a planar N_6 ring with a bond length of 1.32 Å at 100 GPa appears in the structure. These nitrogen hexagons are connected through six N–N bonds with a distance of 1.43 Å and further makeup of the nitrogen network. In contrast, Ne atoms reside in the center of the hexagonal nitrogen unit. Further electron localization function calculation of NeN_6 shows that each nitrogen has a pair of lone electrons, and the electron localization around each N atom is stronger than that of the N–N covalent bond [Fig. S2(a)].

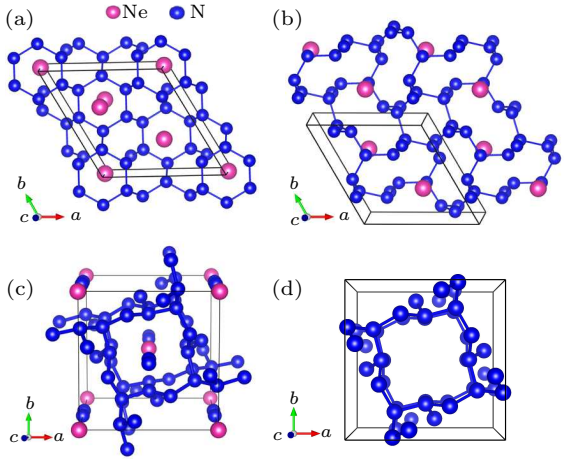

Fig. 2. Crystal structures of Ne–N compounds. (a) $R\bar{3}m$ NeN_6 at 100 GPa. (b) $P6_3/m$ NeN_{10} at 100 GPa. (c) $I4/m$ NeN_{22} at 100 GPa. Host N_{20} consists of a sublattice with $I4/m$ symmetry. Guest Ne atoms constitute a sublattice with space group $I4/mmm$. Guest Ne and N_2 dimers are located in the channel of the host N_{20} structure. (d) The host $I4/m$ N_{20} in $I4/m$ NeN_{22}.

More N-rich NeN_{10} has a hexagonal structure with space group $P6_3/m$ [Fig. 2(b)], in which N atoms have three inequivalent Wyckoff positions ($2d$, $6h$, and $12i$). Each nitrogen atom is located in a tetrahedron formed by three N atoms. Two kinds of nitrogen-nitrogen distances of 1.30 and 1.34 Å are found in the NeN_{10} structure at 100 GPa, which are between the N–N single bond (1.45 Å) and N=N double bond (1.25 Å). Due to the different bond lengths, the N atoms constitute the highly distorted N_{10} rings. Notably, each of the six N_{10} rings contributes one bond with a bond length of 1.30 Å to form a regular hexagon (N_6) in the plane. Furthermore, the bonding feature of the N_6 is further supported by the ELF within the (001) plane (Fig. S2). It is noted that each N in N_6 hexagons have one lone pair of electrons, which reveals that the N_6 has six σ bonds in the sp^2 hybridization state. In addition, some of the N atoms in NeN_{10} show the sp^3 hybridizations or lone pair distribution [Fig. S3(a)]. Moreover, the Ne atoms are interspersed in the framework of N atoms. Such a structural character effectively increases the stability of the NeN_{10} structure.

NeN_{22}, having the highest N content among the predicted Ne–N phases, is a tetragonal host-guest structure with space group $I4/m$ [Fig. 2(c)]. $I4/m$ NeN_{22} consists of $I4/mmm$ Ne and $I4/m$ N sublattices, in which guest atoms (Ne) occupy the $2a$ position of the sublattice with $I4/mmm$ symmetry, whereas N atoms constituting guest N_2 and host N_{20} occupy four inequivalent Wyckoff positions ($8h$, $8e$, $16i$, and $16i$) of N sublattice with space group $I4/m$ N_{22} named t-N_{22}, Interestingly, the obtained host N_{20} structure from NeN_{22}, termed t-N_{20}, still maintains the symmetry of $I4/m$ by removing both Ne and N_2. Notably, t-N_{20} has a channel parallel to the c crystallographic axis [Fig. 2(d)]. In the NeN_{22}, N_2 dimers are symmetrically equivalent. In addition, the bond length in the N_2 is about 1.10 Å, which is similar to that of a triple bond in ϵ-N_2.[58,59] Each atom of N_{20} bonded to the other three N atoms with the distance of 1.33–1.35 Å in the polyatomic network structure. The nearest neighboring Ne and N atoms have distance of approximately 2.08 Å, while the shortest distance between the N_2 dimer and the t-N_{20} is about 2.20 Å. The exotic t-N_{20} framework connects with the surface of irregular N_{12} and N_{10} rings. N_{12} rings with channels parallel to the c-axis, while the bond of the N_2 dimers is also parallel to the c-axis. Such a structural character is conducive to the separation of Ne atoms and N_2 from the channel without destroying the N_{22} frame structure. Because the experiments show that guests may be sufficiently removed to leave behind metastable empty clathrates,[14,61] guest-free Si,Ge-clathrates, and H_2O have indeed been obtained.[9,62,63] Based on the work reported previously, we can not only obtain t-N_{22} by removing guest Ne, but also acquire t-N_{20} via the removal of guest Ne and the N_2 dimer from the natural pores of NeN_{22}. We have optimized the pure tetragonal polymeric nitrogen structures t-N_{22} and t-N_{20} at 1 atm. The final lattice constants of t-N_{22} and t-N_{20} are $a = b = c = 6.0183$ Å and $a = b = c = 5.9487$ Å, respectively, which are smaller than the lattice constants ($a = b = c = 6.0869$ Å) of the NeN_{22} at 1 atm. The lattice constants of t-N_{22} and t-N_{20} are only about 1% and 2% smaller than that of Ne_{22}, respectively. Therefore, the removal of the guest atom from NeN_{22} results in a slight change in the lattice constant. We also observed the effect of pressure on the lattice by calculating the pressure-dependent lattice constants of NeN_{22}, t-N_{22}, and t-N_{20} (Fig. S4). The results show that the lattice constants of NeN_{22}, t-N_{22}, and t-N_{20} gradually decrease with increasing pressure. The lattice constants of t-N_{22} and t-N_{20} are smaller than that of NeN_{22} at high pressure. The ELF shows that NeN_{22} also has lone pairs [Fig. S3(b)]. Overall, they show increased polymerization characteristics with increasing N content. More structural details are listed in Table S1.

These nitrogen-rich $P6_3/m$ NeN_{10} and $I4/m$ NeN_{22} with peculiar structures further motivate us to explore their mechanical properties. Based on the Born stability criteria,[64] the calculated elastic constants via the stress-strain approach[65] of hexagonal $P6_3/m$ NeN_{10} and tetragonal $I4/m$ NeN_{22} verify that they are mechanically stable at ambient pressure (Table S2). Furthermore, their bulk modulus B, shear modulus G, Young's modulus E, and Poisson's ratio ν are calculated using the Voigt–Reuss–Hill approximation.[66] As shown in Table S2, both $P6_3/m$ NeN_{10} and $I4/m$ NeN_{22} have large bulk modulus, shear modulus, Young's modulus, and low Poisson's ratio, indicating that they are stiff materials. Interestingly, based on Gao's model.[67] the Vickers hardness of $P6_3/m$ NeN_{10} is estimated to be 31.3 GPa, which is larger than the high-hardness standard (30 GPa).[68] This result implies that NeN_{10} is also a promising candidate of high-hardness materials. In contrast, the hardness of $I4/m$ NeN_{22} (26.4 GPa) is slightly lower than that of $P6_3/m$ NeN_{10}.

We analyzed the dynamic stabilities of NeN_{10} and NeN_{22} by calculating their phonon spectra at 1 atm [Figs. 3(a) and 3(b)]. Interestingly, there are no negative phonon frequencies below 0 THz in the respective Brillouin zones of NeN_{10} and NeN_{22}, which confirms that they are dynamically stable under ambient pressure. Based on the analysis of the phonon density of states (PHDOS) of NeN_{10} [Fig. S5(a)], we found that the phonon dispersion curve can be split into three groups: low-frequency acoustic modes (below 8 THz), low-frequency optic modes (8–24 THz), and high-frequency optic modes (24–42 THz). The acoustic modes primarily come from the contribution of vibrations of Ne atoms. The low-frequency optic vibrational modes are mainly contributed by the coupled vibrations between Ne and N atoms, while the high-frequency vibrational modes are dominated by N atoms. In contrast, the phonon modes corresponding to N atoms in NeN_{22} dominate the whole frequency region compared to those of Ne atoms, which is closely related to the nitrogen framework. Notably, NeN_{22} has an independent optical branch offered by N atoms at about 75 THz [Fig. S5(b)]. In addition, the absence of imaginary frequencies in the Brillouin zone indicates that $P6_3/m$ NeN_{10} and $I4/m$ NeN_{22} also exhibit good dynamic stability at 100 GPa (Fig. S6). NeN_6 becomes dynamically stable at 100 GPa [Fig. S7(a)]. However, it becomes unstable at 1 atm, so we will not discuss its property further. Meanwhile, we further remove the Ne atoms from the framework of $P6_3/m$ NeN_{10} and $I4/m$ NeN_{22} and explore the naked nitrogen properties. Moreover, the phonon dispersion curves show that the obtained nitrogen structures $P6_3/m$ N_{10}, t-N_{22}, and t-N_{20} remain dynamically sta-

ble under ambient pressure [Fig. S6 in the Supporting Information, and Figs. 3(c) and 3(d)]. Surprisingly, they remain dynamically stable under ambient pressure, in which t-N_{22} and t-N_{20} with peculiar nitrogen structures are our focus.

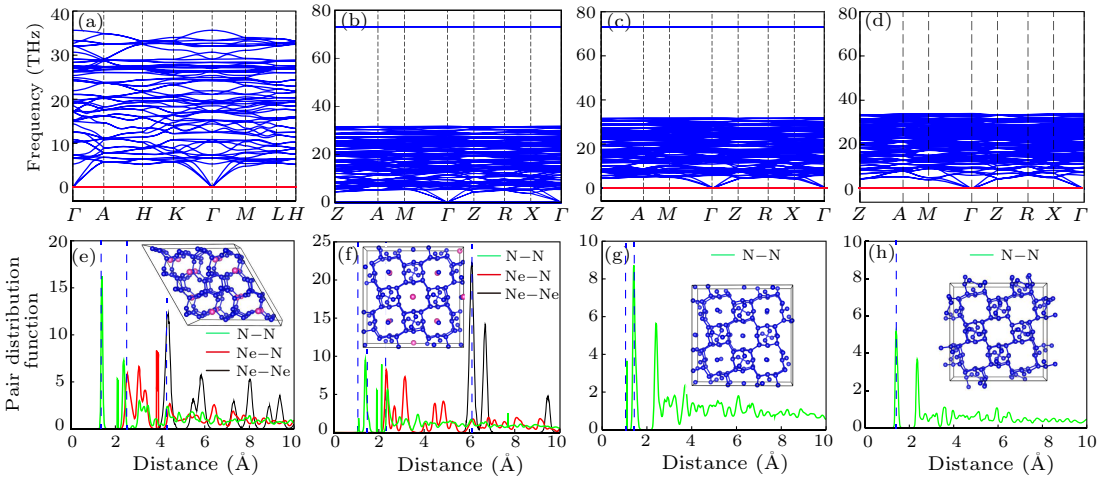

Fig. 3. (a)–(d) Phonon spectra of $P6_3/m$ NeN_{10}, $I4/m$ NeN_{22}, t-N_{22}, and t-N_{20} at ambient pressure, where the horizontal red lines represent 0 THz. (e)–(g) Pair distribution functions of AIMD simulations of NeN_{10}, NeN_{22}, t-N_{22}, and t-N_{20} at 300 K and pressure of 1 atm, wherein the vertical dashed lines represent the nearest or second shortest atomic distances of N–N, Ne–N, and Ne–Ne of the original structure. The terminal structures depicted in the inset graphics were obtained from the last step of molecular dynamics simulations.

To confirm the thermal stability of NeN_{10}, NeN_{22}, t-N_{22}, and t-N_{20}, we performed molecular dynamics simulations at 1 atm and at different temperatures. As shown in Fig. S8, the total energies of these structures have no significant fluctuations with the evolution of time, indicating that they are in equilibrium at considered temperatures. To clearly reveal the efficiency of molecular dynamics simulations, the equilibrium structures were obtained from the last step of AIMD simulations. The radial distribution functions (RDFs) examine the thermal stability of NeN_{10}, NeN_{22}, t-N_{22}, and t-N_{20} under ambient pressure and at 300 K, where the sharp peaks on the far left of each line represent the nearest N–N, Ne–N, and Ne–Ne distances, respectively [Figs. 3(e)–3(h)]. Generally, the closest distances between atoms of equilibrium structure have little change compared to the original structure, proving that this structure is thermally stable. For NeN_{22}, the first sharp peak of RDF is at approximately 1.09 Å, which matches well with the shortest N–N bond length of the N_2 dimer of the original structure (vertical dashed line). The second sharp peak representing the second shortest bond between nitrogen atoms is at 1.39 Å, which is consistent with the second shortest N–N bond length of the original structure. The first sharp peak of Ne–N is at approximately 2.31 Å, which agrees well with the shortest distance between Ne and N atoms of the original structure. Remarkably, the nearest N–N, Ne–N, and Ne–Ne distances have little change compared to those in the initial structures of NeN_{10}, NeN_{22}, t-N_{22}, and t-N_{20}, which implies that they remain solid and keep thermal stability. As also can be seen from the insets in Figs. 3(e)–3(h), the terminal structures (NeN_{10}, NeN_{22}, t-N_{22}, and t-N_{20}) from the last step of the AIMD simulations still retain their structural integrity. Furthermore, we performed the AIMD simulations at higher temperatures by adopting the initial structure. The AIMD simulations for NeN_{10} at 1000 K and NeN_{22} at 500 K [Figs. S9(a) and S9(b)] prove that they are still stable at higher temperatures. The above dynamic and thermal stability analyses of NeN_{10} and NeN_{22} indicate that they can be quenched to ambient conditions once synthesized at high pressure. In addition, we performed AIMD simulations of NeN_{22} at a pressure of 76 GPa and a temperature of 300 K. As shown in Fig. S10(a), there is only a tiny difference in the simulated interatomic distance for the terminal structure compared to the original structure. The result shows that NeN_{22} remains thermally stable at high pressure. In view of the above analysis, we prove that the ambient pressure polymerized nitrogen phases can be synthesized by removing the guest atoms from $I4/m$ NeN_{22}.

The unique crystal structures in NeN_{10} with N_6 and N_{10} rings and NeN_{22} with the N_2 dimers and N_{20} framework further stimulate us to study their electronic properties. Strikingly, the calculated electronic bands and projected density of states (PDOS) of NeN_{10} and NeN_{22} at 1 atm reveal that they are semiconductors with large direct bandgaps of 2.8 and 3.0 eV, respectively (Fig. S11). As pressure in-

creases up to 100 GPa, the increased band gaps of NeN_{10} and NeN_{22} become 3.8 and 4.6 eV, respectively [Figs. S12(a) and 4(a)]. In addition, NeN_{22} was found to have a bandgap of 4.3 eV at an initial thermodynamically stable pressure of 76 GPa [Fig. S10(b)]. As illustrated in PDOS of Fig. S11, the obvious overlap between N s and N p orbitals exists in the valence band region, proving the strong coupling between N atoms and supporting the structural stability. Further, Bader charge analysis shows that the charge transfer from each Ne atom to N atoms in these two structures is less than $0.05|e|$ in NeN_{10} and NeN_{22} at 1 atm (Tables S3 and S4), which indicates that adding Ne has almost no effect on the electronic distribution of the N framework. Additionally, charge transfer could hardly be observed between the Ne and N atoms of NeN_{10} and NeN_{22} with further increasing pressures. However, for NeN_{22}, there are slightly large charge transfers from N_{20} cages to N_2 dimers as pressure increases (Table S4), which indicates that the N atoms in NeN_{22} can act as both cations and anions.

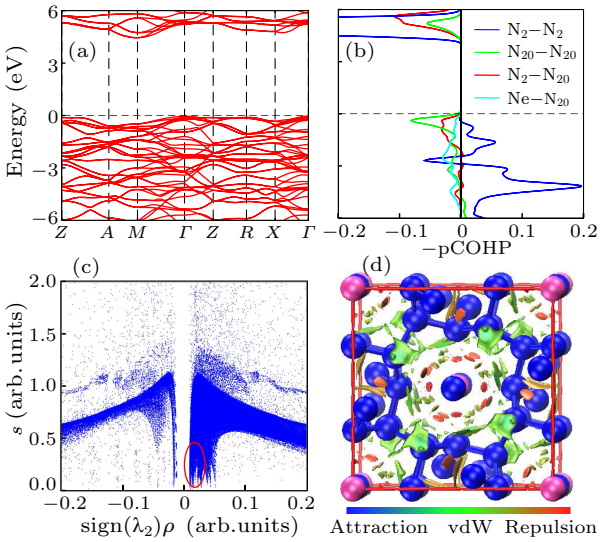

Fig. 4. Electronic properties and the weak noncovalent interactions of $I4/m$ NeN_{22} at 100 GPa. (a) Electronic band structures and (b) the minus projected crystal orbital Hamiltonian population (–pCOHP), where the horizontal dashed line represents the Fermi level. (c) The two-dimensional (2D) and (d) three-dimensional (3D) plots of RDG versus the electron density multiplied by the sign of the second Hessian eigenvalue (λ_2). The solid red line region in (c) represents the vdW interactions in the crystalline.

To investigate the reasons for the bonding characteristics of NeN_{10} and NeN_{22}, we calculated their minus projected COHP (–pCOHP) at 100 GPa, as shown in Figs. 4(b) and S12(b). In general, the positive and negative –pCOHPs characterize the bonding and antibonding states, respectively. The –pCOHP for averaged nitrogen-nitrogen pair (N–N) [Fig. 4(b)] demonstrates that there is a bonding state between nitrogen atoms in the N_2 dimers, while the antibonding interactions between the shortest N–N of N_{20} cage or N_2 dimers and N_{20} cages are both negative in the energy range from −6 to 0 eV below the top of the valence bands. For NeN_{10}, the integrated COHP (ICOHP) values of Ne–N and N–N pairs are 0.01 and −12.90 eV/pair up to the Fermi level, respectively. For NeN_{22}, the ICOHP values of the N–N bond in N_2 dimer and the nearest N–N bond in N_{20} up to the Fermi level are −8.86 and −24.54 eV/pair (Table S5), respectively, which shows that the triple bond in N_2 dimer is stronger than both the single and the double bond in N_{20}. The ICOHP values among N_{20}, Ne, and N_2 dimers are close to 0 eV/pair, further indicating that Ne and N_2 can be removed.

Although the vdW interactions in nitrides bearing noble elements have been studied, there are no quantitative studies on the weak interactions in nitrides bearing noble elements. At the same time, due to the low electron density, the intricate weak noncovalent interactions (NCIs) cannot be identified via some analysis algorithms such as Bader charge transfer and ELF. Therefore, we introduce the reduced density gradient (RDG) to gain additional insight into the stable mechanism of the $P6_3/m$ NeN_{10} and host-guest structure $I4/m$ NeN_{22} at 100 GPa [Figs. S12(c) and 4(c)]. RDG is defined as

$$s = [2(3\pi^2)]^2|\Delta\rho|^{-4/3}, \tag{2}$$

where ρ represents the electron density. To distinguish the different types of interactions, we multiplied RDG by the sign of the second Hessian eigenvalue [sign(λ_2)] of $\Delta 2\rho$. The low-density [sign(λ_2)ρ (arb. units)] and low-gradient [s (arb. units)] spikes indicate the existence of weak interactions. The two-dimensional (2D) and related three-dimensional (3D) graphs of RDG can clearly show the NCI regions [Figs. 4(c), 4(d), S12(c), and S12(d)]. The areas surrounded by solid red lines in 2D graphs of RDG represent the vdW interactions in NeN_{10} and NeN_{22}, corresponding to green contours plotted in 3D graphs of RDG. The cyan and red counters in 3D graphs of RDG display attractive and repulsive interactions, respectively. As seen in Fig. S12(d), the attractive interaction is stronger than the repulsive one around the Ne atoms in NeN_{10}. For NeN_{22}, button-like red contours are located around the Ne atoms and the N_2 dimers, indicating that the repulsive interaction is stronger than the attractive interaction. The results are consistent with the –pCOHP, also indicating that guest atoms can be removed in NeN_{22}.

The decomposition enthalpies of $P6_3/m$ NeN_{10} and $I4/m$ NeN_{22} relative to Ne and nitrogen at ambient pressure are 1.61 and 1.64 eV/atom, respectively, indicating that they are potential high-energy-density materials. Thus, the energy density and explosive performance of NeN_{10} and NeN_{22} are further studied, in

which the energy of nitrogen molecule is adopted.[58,59] NeN_{10} and NeN_{22} can be detonated in the following ways: NeN_{10} (solid) $\rightarrow$ Ne (gaseous) + $5N_2$ (gaseous), NeN_{22} (solid) $\rightarrow$ Ne (gaseous) + $11N_2$ (gaseous). Further calculations show that the energy densities (E_d) of NeN_{10} with density of 3.24 g/cm^3 and NeN_{22} with a density of 3.17 g/cm^3 are estimated to be approximately 11.1 and 11.5 kJ/g, respectively, which are significantly larger than trinitrotoluene (TNT, 4.3 kJ/g) and 1,3,5,7-tetrazoctane (HMX, 5.7 kJ/g).[69] More interestingly, t-N_{22} and t-N_{20} exhibit high-energy densities of 11.6 and 12.0 kJ/g, respectively, which are higher than those of all reported polynitrogen materials. Additionally, as shown in Table 1, we also estimate the explosive performance including detonation velocity (V_d) and pressure (P_d) of $P6_3/m$ NeN_{10}, $I4/m$ NeN_{22}, t-N_{22}, and t-N_{20} through the Kamlet–Jacobs empirical equation.[70] Its validity has been widely confirmed.[71−75] Using these equations, we also calculated detonation velocity and pressure for TNT and HMX, where the monoclinic $P2_1/c$ TNT and $P2_1/c$ HMX are adopted.[76,77] The differences between the calculated and experimental values for TNT and HMX are within acceptable limits (Table 1), indicating that our calculation methods are applicable. The Kamlet–Jacobs empirical equations are as follows:

$$V_d = 1.01(NM^{0.5}E_d^{0.5})^{0.5}(1 + 1.30\rho), \quad (3)$$

$$P_d = 15.58\rho^2 NM^{0.5}E_d^{0.5}. \quad (4)$$

Here, N, M, and ρ represent moles of N_2 per gram of explosives (mol/g), the molar mass for N_2 gas (28 g/mol), and the density (g/cm^3), respectively. A large amount of N_2 is released when NeN_{10} and NeN_{22} explode, resulting in a huge P_d and detonation velocity. We found that NeN_{10} and NeN_{22} release a huge detonation velocity of about 3 times higher than that of TNT and an explosion pressure of about 14 times than that of TNT. Notably, the calculated V_d of t-N_{22} and t-N_{20} (22.82 and 22.09 km/s) are approximately 2 times higher than that of TNT (6.90 km/s) and twice the value of HMX (9.10 km/s).[69,70] $P6_3/m$ NeN_{10}, $I4/m$ NeN_{22}, t-N_{22}, and t-N_{20} can be considered as candidates for high-energy-density materials.

Table 1. Calculated moles of dinitrogen gas per gram of explosives (N), density ρ, energy density E_d, volumetric energy density E_v, detonation velocity V_d, and detonation pressure P_d of NeN_{10}, NeN_{22}, t-N_{22}, and t-N_{20}. For comparison, experimental values for the known TNT and HMX explosives are also listed.[69,78] Herein, superscript expt represents the experimental data.

	N (mol/g)	ρ (g/cm^3)	E_d (kJ/g)	E_v (kJ/cm^3)	V_d (km/s)	P_d (kbar)
NeN_{10}	0.0313	3.24	11.1	35.96	21.96	2848
NeN_{22}	0.0335	3.17	11.5	36.45	22.55	2977
t-N_{22}	0.0357	3.08	11.6	35.72	22.82	3014
t-N_{20}	0.0357	2.92	12.0	35.04	22.09	2764
TNT		1.62	3.9	6.32	6.76	189
TNT^{expt}		1.64	4.3	7.05	6.90	190
HMX		1.90	3.4	6.46	10.1	470
HMX^{expt}		1.90	5.7	10.83	9.10	393

In summary, to obtain high-energy-density Ne-containing nitrides, we have systematically studied Ne–N systems under high pressure by exploiting the first-principles swarm-intelligence structure search and calculated the convex hull of the Ne–N systems at 1 atm, 50 GPa, and 100 GPa. Strikingly, three previously unknown thermodynamically stable Ne–N phases are determined: $R\bar{3}m$ NeN_6, $P6_3/m$ NeN_{10}, and $I4/m$ NeN_{22}. Introducing Ne atoms into a pure nitrogen system can greatly reduce the synthesis pressure to form single and double N bonds compared to the synthesis with pure nitrogen. The predicted structures exhibit various forms of nitrogen: molecular N_2, N_6 ring, N_{10} ring, and N_{20}. Interestingly, the reduced density gradient exhibits the weak non-covalent interactions between the Ne and N atoms, which stabilize the guest atoms within the host framework. In particular, NeN_{10} and NeN_{22} are dynamically and mechanically stable under ambient pressure. Based on the unique structure of $I4/m$ NeN_{22} and weak interactions between host and guest, we propose to remove Ne or Ne and N_2 dimers in NeN_{22} from the natural channels of the structure, and the unique pure tetragonal polymeric nitrogen structures t-N_{22} and t-N_{20} are obtained. Furthermore, the nitrogen framework in NeN_{22} remains dynamically stable under ambient pressure after the removal of the Ne atom or Ne and N_2. The AIMD calculations suggest that NeN_{10} and NeN_{22} are thermally stable up to 1000 and 500 K under ambient pressure, respectively. More importantly, these results indicate that they are potentially quenchable to ambient conditions. The estimated energy density of NeN_{10}, NeN_{22}, t-N_{22}, or t-N_{20} is more than 2 times larger than that of TNT. In addition, the detonation velocity and the detonation pressures of NeN_{10}, NeN_{22}, t-N_{22}, and t-N_{20} are significantly larger than those of TNT and HMX. The results demonstrate that $P6_3/m$ NeN_{10}, $I4/m$ NeN_{22}, t-N_{22}, and t-N_{20} are

promising high-energy-density materials. Our work provides insights into the formation and properties of Ne–N compounds and deepens the understanding of the evolution of planets.

Acknowledgments. This work was supported by the National Key Research and Development Program of China (Grant No. 2021YFA1400400), the Fundamental Research Funds for the Central Universities (Grant No. 020414380185), the Natural Science Foundation of Jiangsu Province (Grant No. BK20200007), the National Natural Science Foundation of China (Grant Nos. 12074181, 11834006, and 11704062), the Fok Ying-Tong Education Foundation of China (Grant No. 161006), and the Fund from Jilin Province (Grant No. JJKH20221152KJ).

References

[1] Guillot T 2005 *Annu. Rev. Earth Planet. Sci.* **33** 493
[2] Vogt M, Trieloff M, Ott U, Hopp J and Schwarz W H 2021 *Commun. Earth Environ.* **2** 1
[3] Dong X, Oganov A R, Goncharov A F *et al.* 2017 *Nat. Chem.* **9** 440
[4] Monserrat B, Martinez-Canales M, Needs R J and Pickard C J 2018 *Phys. Rev. Lett.* **121** 015301
[5] Zhang J, Lv J, Li H, Feng X, Lu C, Redfern S A, Liu H, Chen C and Ma Y 2018 *Phys. Rev. Lett.* **121** 255703
[6] Gao H, Sun J, Pickard C J and Needs R J 2019 *Phys. Rev. Mater.* **3** 015002
[7] Liu Z, Botana J, Hermann A, Valdez S, Zurek E, Yan D, Lin H Q and Miao M S 2018 *Nat. Commun.* **9** 951
[8] Sanloup C, Bonev S A, Hochlaf M and Casely H E M 2013 *Phys. Rev. Lett.* **110** 265501
[9] Falenty A, Hansen T C and Kuhs W F 2014 *Nature* **516** 231
[10] Liu H, Yao Y and Klug D D 2015 *Phys. Rev. B* **91** 014102
[11] Liu C, Gao H, Wang Y, Needs R J, Pickard C J, Sun J, Wang H T and Xing D 2019 *Nat. Phys.* **15** 1065
[12] Lotz H and Schouten J 2001 *Phys. Rev. B* **64** 184101
[13] Kim M and Yoo C S 2011 *J. Chem. Phys.* **134** 044519
[14] Jacobson L C, Hujo W and Molinero V 2009 *Phys. Chem. B* **113** 10298
[15] Peng F, Wang Y, Wang H, Zhang Y and Ma Y 2015 *Phys. Rev. B* **92** 094104
[16] Cotton F A, Wilkinson G, Murillo C A, Bochmann M and Grimes R 1988 *Advanced Inorganic Chemistry* 6 edn (New York: Wiley)
[17] O'Sullivan O T O and Zdilla M J 2020 *Chem. Rev.* **120** 5682
[18] Stierstorfer J and Klapotke T M 2010 *Annu. Rev. Earth Planet.* **33** 493
[19] Mailhiot C, Yang L and McMahan A 1992 *Phys. Rev. B* **46** 14419
[20] Eremets M I, Gavriliuk A G, Trojan I A, Dzivenko D A and Boehler R 2004 *Nat. Mater.* **3** 558
[21] Ma Y, Oganov A R, Li Z, Xie Y and Kotakoski J 2009 *Phys. Rev. Lett.* **102** 065501
[22] Wang X, Wang Y, Miao M, Zhong X, Lv J, Cui T, Li J, Chen L, Pickard C J and Ma Y 2012 *Phys. Rev. Lett.* **109** 175502
[23] Sun J, Martinez-Canales M, Klug D D, Pickard C J and Needs R J 2013 *Phys. Rev. Lett.* **111** 175502
[24] Adeleke A A, Greschner M J, Majumdar A, Wan B, Liu H, Li Z, Gou H and Yao Y 2017 *Phys. Rev. B* **96** 224104
[25] Ji C, Adeleke A A, Yang L, Wan B, Gou H, Yao Y, Li B, Meng Y, Smith J S, Prakapenka V B *et al.* 2020 *Adv.* **6** eaba9206
[26] Laniel D, Winkler B, Fedotenko T, Pakhomova A, Chariton S, Milman V, Prakapenka V, Dubrovinsky L and Dubrovinskaia N 2020 *Phys. Rev. Lett.* **124** 216001
[27] Vaitheeswaran G and Babu K R 2012 *J. Chem. Sci.* **124** 1391
[28] Ji C, Zhang F, Hou D, Zhu H, Wu J, Chyu M C, Levitas V I and Ma Y 2011 *J. Phys. Chem. Solids* **72** 736
[29] Zhang S, Zhao Z, Liu L and Yang G 2017 *J. Power Sources* **365** 155
[30] Liu Z, Li D, Tian F, Duan D, Li H and Cui T 2020 *Inorg. Chem.* **59** 8002
[31] Peng F, Yao Y, Liu H and Ma Y 2015 *J. Phys. Chem. Lett.* **6** 2363
[32] Liu L, Wang D, Zhang S and Zhang H 2021 *J. Mater. Chem. A* **9** 16751
[33] Vos D W, Finger L, Hemley R, Hu J, Mao H and Schouten J 1992 *Nature* **358** 46
[34] Li Y, Feng X, Liu H, Hao J, Redfern S A, Lei W, Liu D and Ma Y 2018 *Nat. Commun.* **9** 722
[35] Hou J, Weng X J, Oganov A R, Shao X, Gao G, Dong X, Wang H T, Tian Y and Zhou X F 2021 *Phys. Rev. B* **103** L060102
[36] Plisson T, Weck G and Loubeyre P 2014 *Phys. Rev. Lett.* **113** 025702
[37] Wang Y, Lv J, Zhu L and Ma Y 2010 *Phys. Rev. B* **82** 094116
[38] Wang Y, Lv J, Zhu L and Ma Y 2012 *Comput. Phys. Commun.* **183** 2063
[39] Zhu L, Wang H, Wang Y, Lv J, Ma Y, Cui Q, Ma Y and Zou G 2011 *Phys. Rev. Lett.* **106** 145501
[40] Lv J, Wang Y, Zhu L and Ma Y 2011 *Phys. Rev. Lett.* **106** 015503
[41] Miao M S 2013 *Nat. Chem.* **5** 846
[42] Liu L, Zhao Z, Yu T, Zhang S, Lin J and Yang G 2018 *J. Phys. Chem. C* **122** 6801
[43] Perdew J P, Burke K and Ernzerhof M 1996 *Phys. Rev. Lett.* **77** 3865
[44] Kresse G and Furthmuller J 1996 *Phys. Rev. B* **54** 11169
[45] Blochl P E 1994 *Phys. Rev. B* **50** 17953
[46] Pack J D and Monkhorst H J 1977 *Phys. Rev. B* **16** 1748
[47] Parlinski K, Li Z and Kawazoe Y 1997 *Phys. Rev. Lett.* **78** 4063
[48] Togo A and Tanaka I 2015 *Scr. Mater.* **108** 1
[49] Grimme S, Antony J, Ehrlich S and Krieg H 2010 *J. Chem. Phys.* **132** 154104
[50] Grimme S, Ehrlich S and Goerigk L 2011 *J. Comput. Chem.* **32** 1456
[51] Parrinello M and Rahman A 1980 *Phys. Rev. Lett.* **45** 1196
[52] Becke A D and Edgecombe K E 1990 *J. Chem. Phys.* **92** 5397
[53] Dronskowski R and Blochl P E 1993 *J. Chem. Phys.* **97** 8617
[54] Maintz S, Deringer V L, Tchougreeff A L and Dronskowski R 2016 J. Comput. Chem. **37** 1030
[55] Mori-Sanchez H, Contreras J, Cohen A J and Yang W 2010 *J. Am. Chem. Soc.* **132** 6498
[56] Otero-de-la-Roza A, Johnson E R and Luaña V 2014 *Comput. Phys. Commun.* **185** 1007
[57] Humphrey W, Dalke A and Schulten K 1996 *J. Mol. Graph.* **14** 33
[58] Bini L R, Ulivi L, Kreutz J and Jodl H J 2000 *J. Chem. Phys.* **112** 8522
[59] Pickard C J and Needs R 2009 *Phys. Rev. Lett.* **102** 125702
[60] He Y G, Tang X Z and Pu Y K 2010 *Physica B* **405** 4335
[61] Wooldridge P J, Richardson H H and Devlin J P 1987 *J. Chem. Phys.* **87** 4126
[62] Gryko J, McMillan P F, Marzke R F, Ramachandran G K, Patton D, Deb S K and Sankey O F 2000 *Phys. Rev. B* **62** R7707

[63] Guloy A M and Ramlau R 2006 *Nature* **443** 320
[64] Wu Z J, Zhao E J, Xiang H P, Hao X F, Liu X J and Meng J 2007 *Phys. Rev. B* **76** 054115
[65] Page Y L and Saxe P 2002 *Phys. Rev. B* **65** 104104
[66] Hill R 1952 *Proc. Phys. Soc. Sect. A* **65** 349
[67] Gao F 2006 *Phys. Rev. B* **73** 132104
[68] Gale W F and Totemeier T C 2003 *Smithells Metals Reference Book* (Amsterdam: Elsevier)
[69] Dobratz and Brigitta M 1985 *OSTI.GOV/Technical Report: LLNL Explosives Handbook: Properties of Chemical Explosives and Explosives and Explosive Simulants* (CA: Lawrence Livermore National Lab)
[70] Kamlet M J and Dickinson C 1968 *J. Chem. Phys.* **48** 43
[71] Zhang Y, Guo Y, Joo Y H, Parrish D A and Shreeve J M 2010 *Chem. Eur. J.* **16** 10778
[72] Galvez-Ruiz J C, Holl G, Karaghiosoff K, Klapotke T M *et al.* 2005 *Inorg. Chem.* **44** 4237
[73] Klapotke T M 2019 *Chemistry of High-Energy Materials* (Boston: de Gruyter)
[74] Yuan J, Xia K, Wu J and Sun J 2021 *Sci. Chin.: Phys. Mech. Astron.* **64** 1
[75] Li C, Li H, Zong H H, Huang Y, Gozin M, Sun C Q and Zhang L 2020 *iScience* **23** 100944
[76] Vrcelj R M, Sherwood J N, Kennedy A R, Gallagher H G and Gelbrich T 2003 *Cryst. Growth* **3** 1027
[77] Choi C S and Boutin H P 1970 *Acta Crystallogr. B* **26** 1235
[78] Xia K, Yuan J, Zheng X, Liu C, Gao H, Wu Q and Sun J 2019 *J. Phys. Chem. Lett.* **10** 6166

Supporting Information： Pressure-driven Ne-bearing Polynitrides with Ultrahigh Energy Density

Lulu Liu(刘璐璐)[1,2], Shoutao Zhang(张守涛)[3,*], and Haijun Zhang(张海军)[1,2,†]

[1]*National Laboratory of Solid State Microstructures, School of Physics, Nanjing University, Nanjing 210093, China*

[2]*Collaborative Innovation Center of Advanced Microstructures, Nanjing University, Nanjing 210093, China*

[3]*Centre for Advanced Optoelectronic Functional Materials Research and Key Laboratory for UV Light-Emitting Materials and Technology of Ministry of Education, Northeast Normal University, Changchun 130024, China*

Address correspondence to: *zhangst966@nenu.edu.cn; †zhanghj@nju.edu.cn

Index **Page**

S1. Computational details ……2

1. The formation enthalpy of $P6_3/m$ NeN_{10} relative to NeN_6 or Ne and N_2 ……3

2. Electron localization function (ELF) of NeN_6 and NeN_{10} at 100 GPa ……3

3. The ELF isosurface of $P6_3/m$ NeN_{10} and $I4/m$ NeN_{22} at 100 GPa ……3

4. Pressure dependence of lattice constants of NeN_{22}, *t*-N_{22}, and *t*-N_{20} ……4

5. Phonon density of states of $P6_3/m$ NeN_{10} and $I4/m$ NeN_{22} at 1atm ……4

6. Phonon dispersion of N_{10}, $N_{22,}$ NeN_{10}, and NeN_{22} ……4

7. Dynamical and thermal stability of *R*-3*m* NeN_6 at 100 GPa ……5

8. The molecular dynamics of the Ne-N compounds ……5

9. *Ab initio* molecular dynamics (AIMD) of $P6_3/m$ NeN_{10} and $I4/m$ NeN_{22} ……6

10. Thermal stability and electronic band structure of NeN_{22} at 76 GPa ……6

11. Electronic band structure and PDOS of $P6_3/m$ NeN_{10} and $I4/m$ NeN_{22} at 1 atm ……7

12. Electronic properties and weak noncovalent interactions of NeN_{10} at 100 GPa …7

13. Structural information of predicted Ne-N compounds ……8

14. Calculated elastic constant of Ne-N compounds at ambient pressure ……9

15. Charge transfer in $P6_3/m$ NeN_{10} at selected pressures ……9

16. Charge transfer in $I4/m$ NeN_{22} at selected pressures ……9

17. The ICOHP values of the $I4/m$ NeN_{22} at 1 atm ……9

18. Structural information of predicted Ne-N compounds (vasp) ……10

19. References ……14

Computational Details

We employed the unbiased swarm intelligence structure prediction method as implemented in CALYPSO code.[1,2] In the first step, random structures with certain symmetry are constructed in which atomic coordinates are generated by the crystallographic symmetry operations. Local optimizations using the VASP code[3] were done with the conjugate gradients method and stopped when enthalpy changes became smaller than 1×10^{-5} eV per cell. After processing the first generation structures, 60% of them with lower enthalpies are selected to construct the next generation structures by PSO (Particle Swarm Optimization). 40% of the structures in the new generation are randomly generated. A structure fingerprinting technique of bond characterization matrix is applied to the generated structures, so that identical structures are strictly forbidden. These procedures significantly enhance the diversity of the structures, which is crucial for structural global search efficiency.

On the basis of Born stability criteria[4], the elastic constants for a tetrahedral structure should satisfy the generalized elastic stability criteria. The mechanical stablility criteria for hexagonal phase:$C_{44}>0$, $C_{11}>|C_{12}|$, $(C_{11}+2C_{12})*C_{33} > 2C_{13}^2$. The mechanical stablility criteria for tetragonal phase: $C_{11} > 0$, $C_{33} > 0$, $C_{44} > 0$, $C_{66} > 0$, $C_{11} - C_{12} > 0$, $C_{11} + C_{33} - 2C_{13} > 0$, $2(C_{11}+C_{12}) + C_{33} + 4C_{13} > 0$. The Vickers hardness was estimated using an empirical model $H_v = 2.0(k^2G)^{0.585} - 3.0$, where $k = G/B$. Here G and B are shear modulus and bulk modulus, respectively. We also calculate detonation velocity and pressure for TNT and HMX. The TNT and HMX are to be detonated under ideal conditions in the following ways :

For TNT: $2C_7H_5N_3O_6 \rightarrow 3N_2$ (g) + 7CO (g) + $5H_2O$ (g) + 7C (s) + Energy

For HMX: $C_4H_8N_8O_8 \rightarrow 4N_2$ (g) + 4CO (g) + 4H2O (g) + Energy

Here, we adopt the $P2_1/c$ $C_7H_5N_3O_6$, $P2_1/c$ $C_4H_8N_8O_8$, α-nitrogen, $P2_12_12_1$ CO, $Cmc2_1$ H_2O, R-3m graphite to calculate the explosive performance.

Supporting Figures

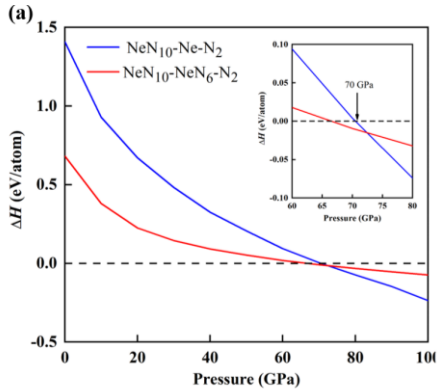

Figure S1. (a) The formation enthalpies (ΔH) calculated with inclusion of DFT-D3 functional of $P6_3/m$ NeN_{10} relative to the mixtures of R-3m NeN_6 or neon and nitrogen phases.

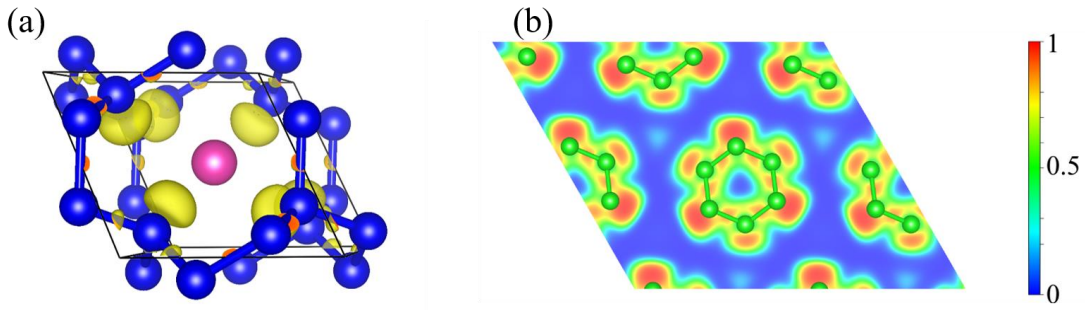

Figure S2. (a) The electron localization function of R-3m NeN_6 at isosurface level of 0.87 under 100 GPa. (b)The ELF of $P6_3/m$ NeN_{10} within the (0 0 1) plane at 100 GPa, here, the green spheres represent N atoms

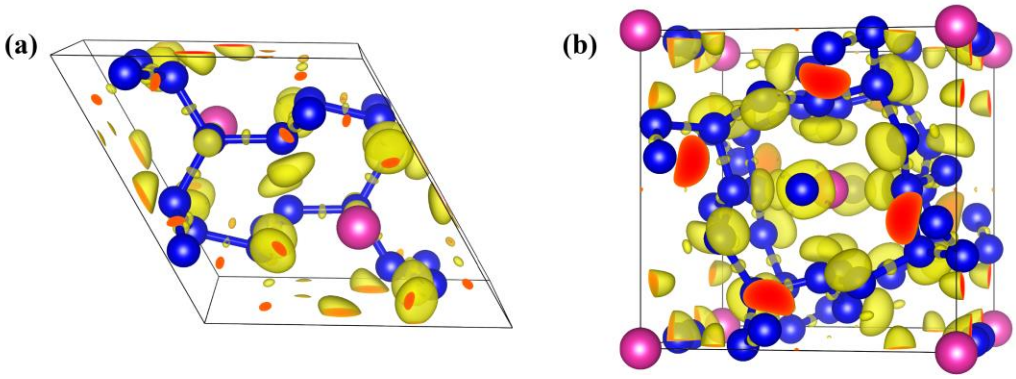

Figure S3. The calculated ELF isosurfaces of (a) $P6_3/m$ NeN_{10} and (b) $I4/m$ NeN_{22} at ELF = 0.87 under 100 GPa.

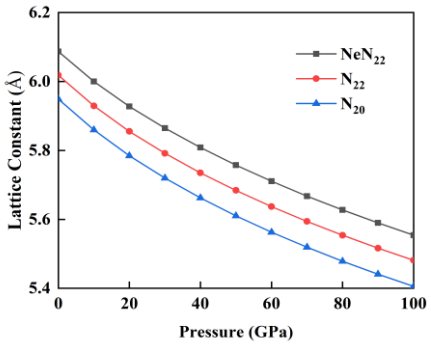

Figure S4. Pressure dependence of lattice constants of NeN_{22}, *t*-N_{22}, and *t*-N_{20}.

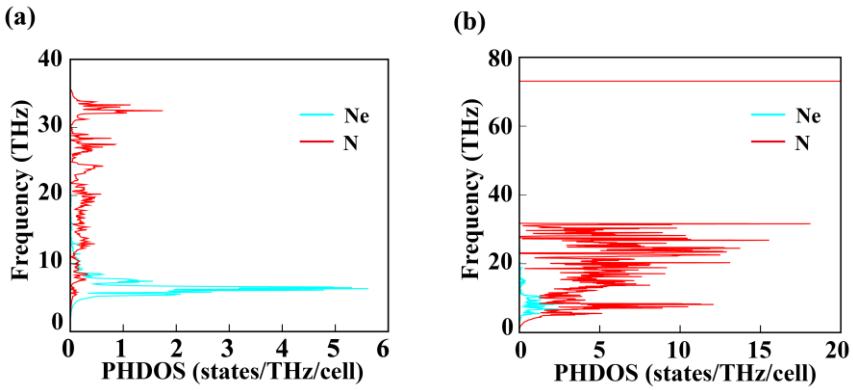

Figure S5. Phonon density of states of (a) *P*6$_3$/*m* NeN_{10} and (b) *I*4/*m* NeN_{22} at 1atm.

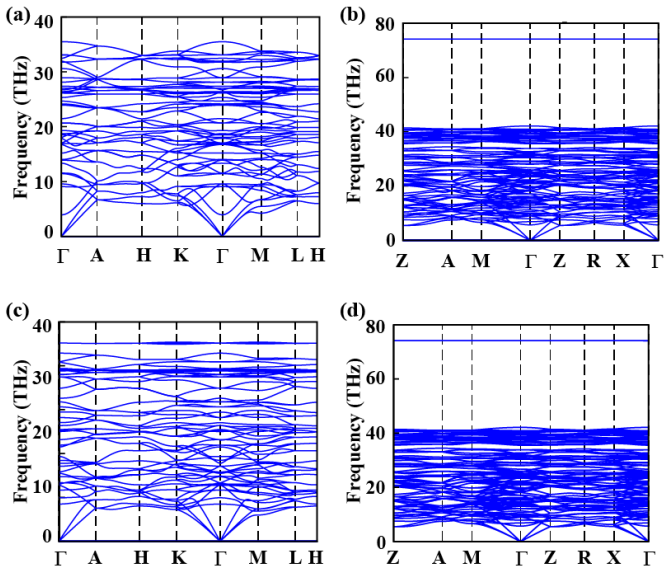

Figure S6. (a) Phonon dispersion of NeN_{10} without Ne atoms (*P*6$_3$/*m* N_{10}) at 1atm. (b) Phonon dispersion of NeN_{22} without Ne atoms (*I*4/*m* N_{22}) at 100 GPa. (c)-(d) Phonon dispersion of *P*6$_3$/*m* NeN_{10} and *I*4/*m* NeN_{22} at 100 GPa.

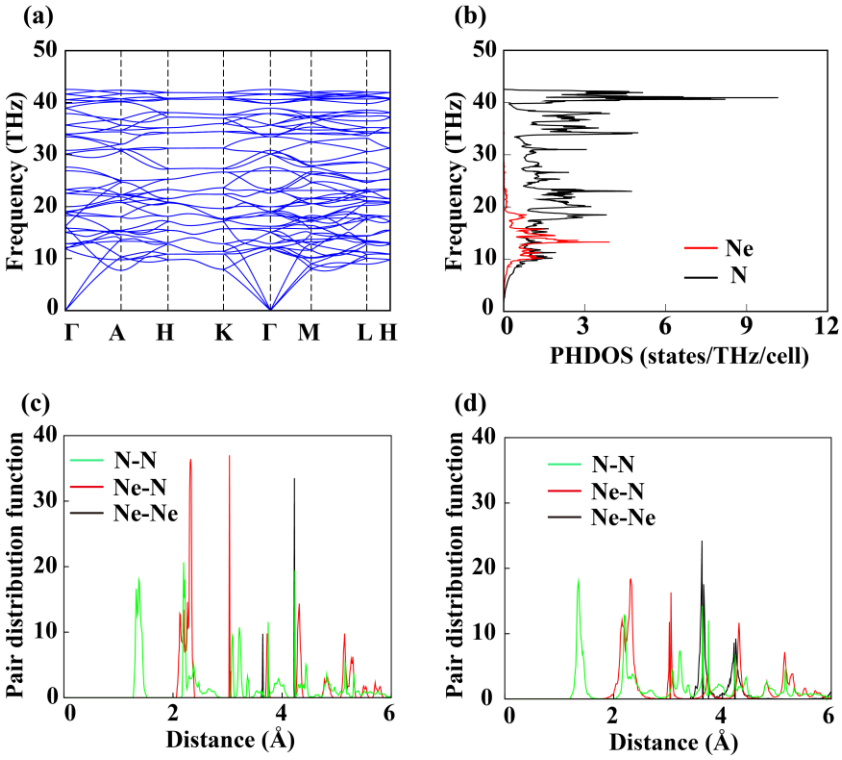

Figure S7. Dynamical and thermal stability of *R*-3*m* NeN_6 at 100 GPa. (a) Phonon dispersion and (b) phonon density of states (PHDOS) projected on Ne and N atoms. (c)-(d) Pair distribution functions of AIMD simulations at temperatures of 300 and 1000 K, where the green, red, and black lines represent the N-N, Ne-N, and Ne-Ne pairs, respectively.

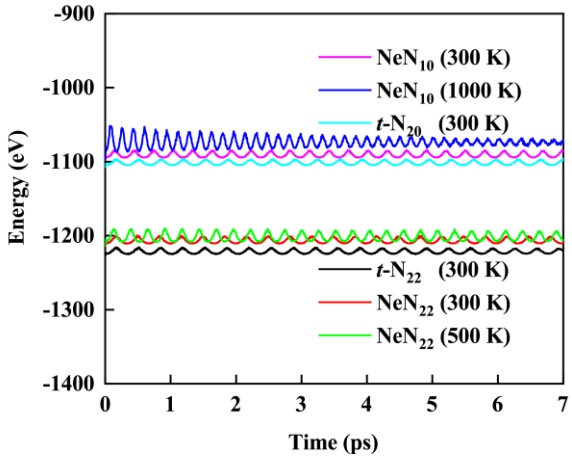

Figure S8. Molecular dynamics simulation of *P*6$_3$/*m* NeN_{10}, *I*4/*m* NeN_{22}, *t*-N22, and N_{20} at ambient pressure and different temperatures.

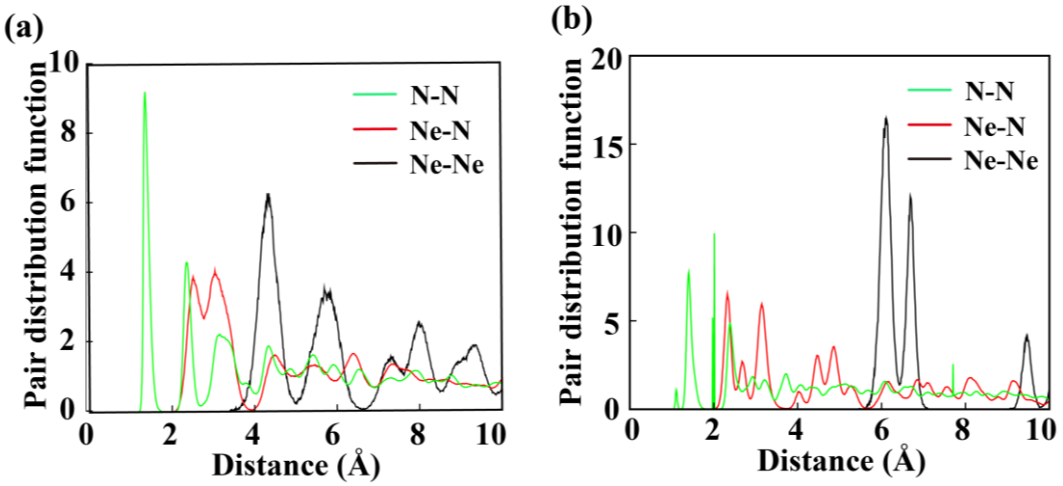

Figure S9. (a) AIMD simulations of *P*6$_3$/*m* NeN_{10} at temperatures of 1000 K at 1 atm and (b) AIMD simulations of *I*4/*m* NeN_{22} at temperatures of 500 K at 1atm, where the green, red, and black lines represent the N-N, Ne-N, and Ne-Ne pairs, respectively.

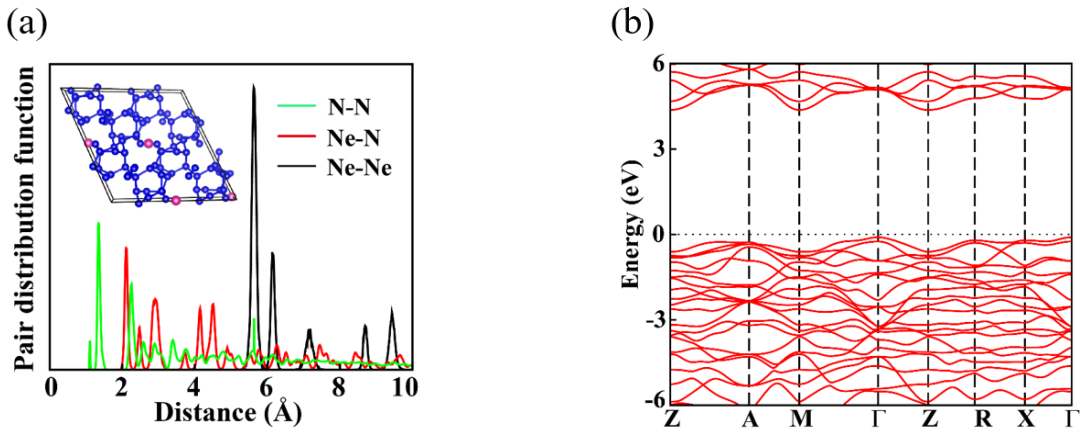

Figure S10. (a) Pair distribution functions of *ab initio* molecular dynamics (AIMD) simulations of NeN_{22} at a pressure of 76 GPa and temperature of 300 K. (b) Electronic band structure of NeN_{22} at 76 GPa.

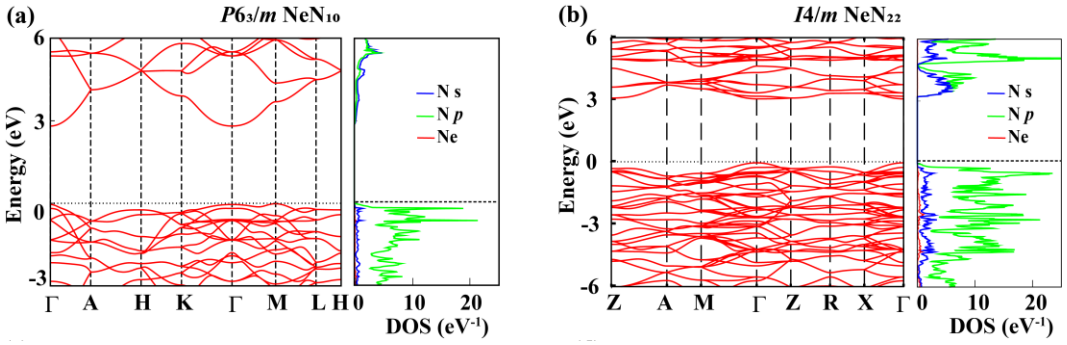

Figure S11. Electronic band structure and PDOS of (a) *P*6$_3$/*m* NeN_{10} and (b) *I*4/*m* NeN_{22} at 1 atm, where, the horizontal dashed lines represent the Fermi level.

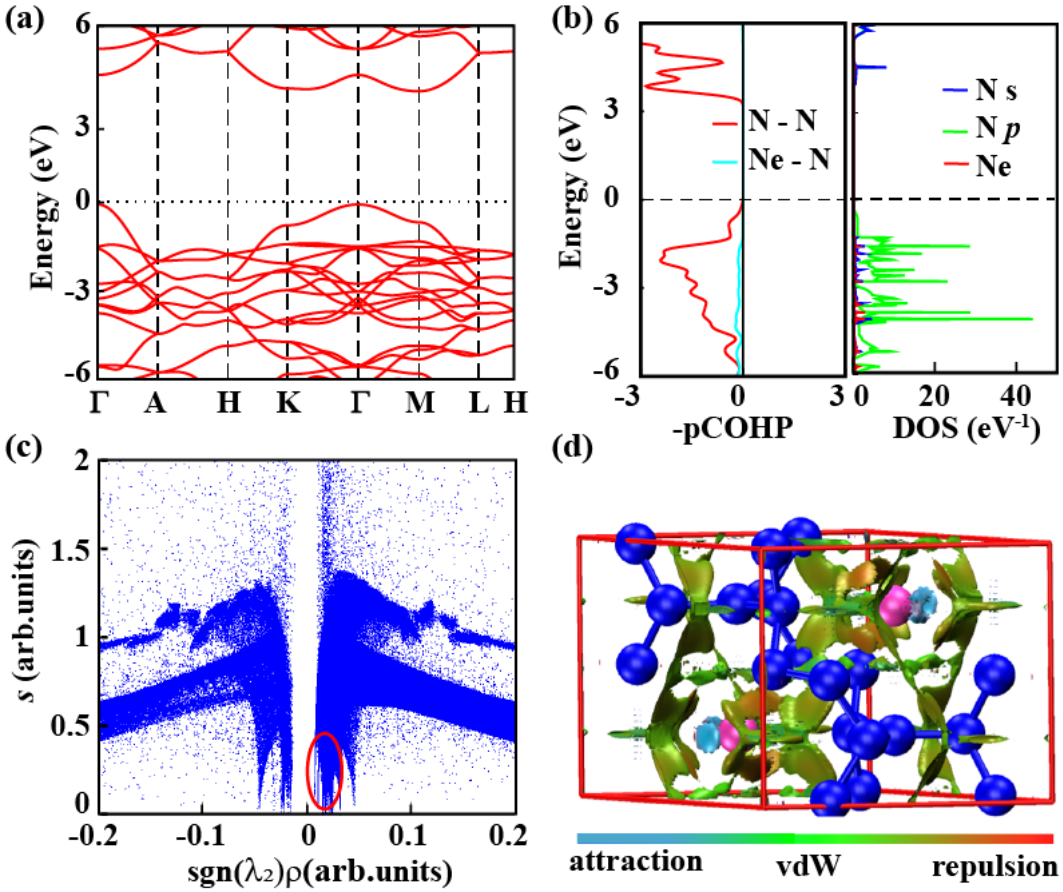

Figure S12. Electronic properties and the weak noncovalent interactions of *P*6$_3$/*m* NeN_{10} at 100 GPa. (a) Electronic band structures, (b) the projected crystal orbital Hamiltonian population (pCOHP) (left), and PDOS (right), where the horizontal dashed line represents the Fermi level. (c) and (d) 2D and 3D plots of RDG versus the electron density multiplied by the sign of the second Hessian eigenvalue (λ_2).

Table S1. Structural parameters of predicted stable Ne-N compounds, *I*4/*m* N_{22}, and *P*6_3/*m* N_{10} at selected pressures.

Phases	Pressure	Lattice Parameters (Å, °)	Atoms	Wyckoff Positions (fractional) *x*	*y*	*z*
***I*4/*m* NeN_{22}**	100 GPa	*a* = 6.0680	Ne(2a)	0.0000	0.0000	0.0000
		b = 6.0680	N1(16i)	0.2009	0.3407	0.2073
		c = 7.0528	N2(16i)	0.2903	0.0023	0.1564
		α = 90	N3(8h)	0.1014	0.4373	0.5000
		β = 90	N4(4e)	0.0000	0.0000	0.42175
		γ = 90				
***P*6$_3$/*m* NeN_{10}**	100 GPa	*a* = 5.4011	Ne(2c)	0.3333	0.6667	0.2500
		b = 5.4011	N1(12i)	0.2067	0.9342	0.5169
		c = 4.7990	N2(6h)	0.67401	0.0961	0.2500
		α= 90	N3(2d)	0.6667	0.3333	0.2500
		β = 90				
		γ = 120				
***R*-3*m* NeN_6**	100 GPa	*a* = 5.9164	Ne(3b)	0.0000	0.0000	0.5000
		b = 5.9164	N1(18h)	0.7950	0.20493	0.3261
		c = 3.7465				
		α= 90				
		β = 90				
		γ = 120				
***Cmcm* NeN_4**	50 GPa	*a* = 4.4181	Ne(4c)	0.0000	0.1075	1.2500
		b = 9.6992	N1(8f)	0.5000	0.0496	0.9574
		c = 6.5836	N2(8f)	0.0000	0.2022	0.8345
		α=*β*=*γ*=90				
***I*4/*m* N_{22}**	1 atm	*a* = 6.5723	N1(16i)	0.0000	0.7063	0.15436
		b = 6.5723	N2(16i)	0.3420	0.8050	0.2154
		c = 7.6667	N3(8h)	0.4502	0.8969	0.5000
		α =*β* =*γ* = 90	N4(4e)	0.0000	0.0000	0.4277
***I*4/*m* N_{20}**	1 atm	*a* = 6.4508	N1(16i)	0.9976	0.7084	0.15281
		b = 6.4508	N2(16i)	0.3440	0.7990	0.2129
		c = 7.6547	N3(8h)	0.4496	0.8957	0.5000
		α = 90				
		β = 90				
		γ = 90				
***P*6$_3$/*m* N_{10}**	1 atm	*a* = 5.8745	N1(12i)	0.1607	0.8909	0.5269
		b = 5.8745	N2(6h)	0.7497	0.1518	0.2500
		c = 5.4916	N3(2d)	0.6667	0.3333	0.2500
		α= 90				
		β = 90				
		γ = 120				

Table S2. Calculated elastic constant C_{ij} (GPa), bulk modulus B (GPa) and shear modulus G (GPa), Young's modulus (E), and Poison's ratio (v) of Ne-N compounds at ambient pressure.

	C_{11}	C_{33}	C_{44}	C_{66}	C_{12}	C_{13}	B	G	E	v
P*6$_3$/*m **NeN_{10}**	442.350	379.686	199.374	175.307	91.7364	107.174	208	177	414	0.17
I*4/*m **NeN_{22}**	356.667	471.104	158.503	103.341	43.1773	81.000	174	144	340	0.18

Table S3. Charge transfer in *P*6$_3$/*m* NeN_{10} at selected pressures.

Pressure (GPa)	**Ne Charge (|e|)**	**N cage Charge (|e|)**
1 atm	0.05	-0.05
20	0.05	-0.05
40	0.05	-0.05
60	0.05	-0.05
80	0.05	-0.05
100	0.05	-0.05

Table S4. Charge transfer in *I*4/*m* $(NeN_2)^{\delta-}N_{20}^{\delta+}$ at selected pressures.

Pressure (GPa)	**Ne Charge (|e|)**	**N_2 dimer Charge (|e|)**	**N_{20} cage Charge (|e|)**
1 atm	0.05	0.07	-0.12
20	0.05	0.09	-0.14
40	0.05	0.10	-0.15
60	0.05	0.12	-0.17
80	0.05	0.13	-0.18
100	0.05	0.15	-0.20

Table S5. The ICOHP values for the shortest Ne-N and N-N bonds of the *I*4/*m* NeN_{22} at 1 atm. Here, the unit of ICOHP value is eV/pair.

	Ne-N_{20}	**Ne-N_2**	**N_2-N_{20}**	**N_{20}-N_{20}**	**N_2-N_2**
I*4/*m **NeN_{22}**	-0.02	-0.00	-0.04	-8.86	-24.54

NeN_{22}(vasp)

1.000000

-3.34634995460000	3.34634995460000	3.85025000570000
3.34634995460000	-3.34634995460000	3.85025000570000
3.34634995460000	3.34634995460000	-3.85025000570000

Ne N

1 22

DIRECT

0.0000000000000000	0.0000000000000000	0.0000000000000000	Ne1
0.8559500429999998	0.1555100085000000	0.6996200235000000	N1
0.1440499570000002	0.8444899915000001	0.3003799765000000	N2
0.4558899850000000	0.1563300194999998	0.3003799765000001	N3
0.5441100150000000	0.8436699805000001	0.6996200234999999	N4
0.1555100085000000	0.4558899850000000	0.2995599655000002	N5
0.8444899915000001	0.5441100150000000	0.7004400344999998	N6
0.1563300194999998	0.8559500429999998	0.7004400344999999	N7
0.8436699805000001	0.1440499570000002	0.2995599655000001	N8
0.0241800024999999	0.5592399915000000	0.1519200209999999	N9
0.9758199975000001	0.4407600084999999	0.8480799790000001	N10
0.4073199705000001	0.8722599814999999	0.8480799790000000	N11
0.5926800294999999	0.1277400185000000	0.1519200210000000	N12
0.5592399915000000	0.4073199705000001	0.5350599890000001	N13
0.4407600084999999	0.5926800294999999	0.4649400109999999	N14
0.8722599814999999	0.0241800024999999	0.4649400109999998	N15
0.1277400185000000	0.9758199975000001	0.5350599890000002	N16
0.3988400100000000	0.9512100070000000	0.3500500170000000	N17
0.6011599900000000	0.0487899929999999	0.6499499830000000	N18
0.9512100070000000	0.6011599900000000	0.5523699970000000	N19
0.0487899929999999	0.3988400100000000	0.4476300030000000	N20
0.4279899750000001	0.4279899750000001	0.0000000000000000	N21
0.5720100250000000	0.5720100250000000	0.0000000000000000	N22

NeN_{10} (vasp)

1.000000

5.86116364021186	0.00000000000000	0.00000000000000
-2.93058182010593	5.07591660816114	0.00000000000000
0.00000000000000	0.00000000000000	5.47642278515712

Ne	N
2	20

DIRECT

0.3333333333333333	0.6666666666666665	0.2500000000000000	Ne1
0.6666666666666667	0.3333333333333334	0.7500000000000000	Ne2
0.7470361778622836	0.1495047660880580	0.2500000000000000	N1
0.5975314117742256	0.7470361778622836	0.7500000000000000	N2
0.8504952339119420	0.5975314117742255	0.2500000000000000	N3
0.2529638221377164	0.8504952339119420	0.7500000000000000	N4
0.4024685882257744	0.2529638221377165	0.2500000000000000	N5
0.1495047660880581	0.4024685882257745	0.7500000000000000	N6
0.1624597549607998	0.8925972034791607	0.5268615185350906	N7
0.2698625514816391	0.1624597549607998	0.0268615185350907	N8
0.1074027965208393	0.2698625514816391	0.5268615185350906	N9
0.8375402450392002	0.1074027965208393	0.0268615185350907	N10
0.7301374485183609	0.8375402450392002	0.5268615185350906	N11
0.8925972034791607	0.7301374485183609	0.0268615185350907	N12
0.8375402450392002	0.1074027965208393	0.4731384814649094	N13
0.7301374485183609	0.8375402450392002	0.9731384814649094	N14
0.8925972034791607	0.7301374485183609	0.4731384814649094	N15
0.1624597549607998	0.8925972034791607	0.9731384814649094	N16
0.2698625514816391	0.1624597549607998	0.4731384814649094	N17
0.1074027965208393	0.2698625514816391	0.9731384814649094	N18
0.6666666666666667	0.3333333333333334	0.2500000000000000	N19
0.3333333333333333	0.6666666666666667	0.7500000000000000	N20

N_{22} (vasp)

1.000000

-3.28618750378389	3.28618750378389	3.83324793391826
3.28618750378389	-3.28618750378389	3.83324793391826
3.28618750378389	3.28618750378389	-3.83324793391826

N

22

DIRECT

0.8608881467276626	0.1539477908372404	0.7061189880729584	N1
0.1391118532723374	0.8460522091627596	0.2938810119270416	N2
0.4478288027642821	0.1547691586547042	0.2938810119270416	N3
0.5521711972357179	0.8452308413452958	0.7061189880729584	N4
0.1539477908372404	0.4478288027642821	0.2930596441095779	N5
0.8460522091627596	0.5521711972357179	0.7069403558904221	N6
0.1547691586547042	0.8608881467276626	0.7069403558904221	N7
0.8452308413452958	0.1391118532723374	0.2930596441095779	N8
0.0204703593283329	0.5574280404020342	0.1471041393928062	N9
0.9795296406716671	0.4425719595979659	0.8528958606071938	N10
0.4103239010092280	0.8733662199355268	0.8528958606071939	N11
0.5896760989907720	0.1266337800644733	0.1471041393928061	N12
0.5574280404020342	0.4103239010092280	0.5369576810737013	N13
0.4425719595979659	0.5896760989907720	0.4630423189262987	N14
0.8733662199355268	0.0204703593283329	0.4630423189262988	N15
0.1266337800644733	0.9795296406716671	0.5369576810737012	N16
0.3968812154411210	0.9501961833644175	0.3470773988055385	N17
0.6031187845588790	0.0498038166355825	0.6529226011944615	N18
0.9501961833644175	0.6031187845588790	0.5533149679232965	N19
0.0498038166355825	0.3968812154411210	0.4466850320767035	N20
0.4277035590555965	0.4277035590555965	0.0000000000000000	N21
0.5722964409444034	0.5722964409444034	0.0000000000000000	N22

N_{20} (vasp)

1.000000

-3.22539492653971	3.22539492653971	3.82734138568312
3.22539492653971	-3.22539492653971	3.82734138568312
3.22539492653971	3.22539492653971	-3.82734138568312

N

20

DIRECT

0.8612308432499919	0.1503747444790539	0.7059840067887275	N1
0.1387691567500081	0.8496252555209461	0.2940159932112725	N2
0.4443907376903264	0.1552468364612644	0.2940159932112725	N3
0.5556092623096736	0.8447531635387355	0.7059840067887275	N4
0.1503747444790539	0.4443907376903264	0.2891439012290620	N5
0.8496252555209461	0.5556092623096736	0.7108560987709380	N6
0.1552468364612644	0.8612308432499919	0.7108560987709380	N7
0.8447531635387355	0.1387691567500081	0.2891439012290620	N8
0.0118642515746599	0.5568811900273021	0.1430091376363291	N9
0.9881357484253401	0.4431188099726980	0.8569908623636708	N10
0.4138720523909729	0.8688551139383308	0.8569908623636709	N11
0.5861279476090271	0.1311448860616693	0.1430091376363292	N12
0.5568811900273021	0.4138720523909729	0.5450169384526422	N13
0.4431188099726980	0.5861279476090271	0.4549830615473578	N14
0.8688551139383308	0.0118642515746599	0.4549830615473579	N15
0.1311448860616693	0.9881357484253401	0.5450169384526422	N16
0.3956952744291833	0.9496398574492992	0.3453351318784826	N17
0.6043047255708167	0.0503601425507007	0.6546648681215174	N18
0.9496398574492992	0.6043047255708166	0.5539445830201160	N19
0.0503601425507007	0.3956952744291833	0.4460554169798840	N20

References

[1] Wang, Y.; Lv, J.; Zhu, L.; Ma, Y.. **2012**, *183*, 2063.

[2] Wang, Y.; Lv, J.; Zhu, L.; Ma, Y. *Phys. Rev. B* **2010**, *82*, 094116.

[3] Kresse, G.; Furthmiiller, J. *Comput. Mater. Sci.* **1996**, *6*, 15–50.

[4] Wu, Z.; Zhao, E.; Xiang, H.; Hao, X.; Liu, X.; Meng, J. Phys. Rev. B: Condens. Matter Mater. Phys. 2007, 76, 054115.